Biomaterials 30 (2009) 2864–2872

Contents lists available at ScienceDirect

Biomaterials

journal homepage: www.elsevier.com/locate/biomaterials

Zinc incorporation into hydroxylapatite

Yuanzhi Tang [a,1], Helen F. Chappell [b], Martin T. Dove [b], Richard J. Reeder [a], Young J. Lee [c,*]

[a] Department of Geosciences and Center for Environmental Molecular Science, State University of New York, Stony Brook, NY 11794-2100, USA
[b] Department of Earth Sciences, University of Cambridge, Downing Street, Cambridge CB2 3EQ, UK
[c] Department of Earth and Environmental Sciences, Korea University, Seoul 136-701, Republic of Korea

ARTICLE INFO

Article history:
Received 3 November 2008
Accepted 13 January 2009
Available online 12 February 2009

Keywords:
Hydroxylapatite
Apatite
Bone
Zinc
Density function theory
X-ray absorption spectroscopy

ABSTRACT

By theoretical modeling and X-ray absorption spectroscopy, the local coordination structure of Zn incorporated into hydroxylapatite was examined. Density function theory (DFT) calculations show that Zn favors the Ca2 site over the Ca1 site, and favors tetrahedral coordination. X-ray absorption near edge structure (XANES) spectroscopy results suggest one dominant coordination environment for the incorporated Zn, and no evidence was observed for other Zn-containing phases. Extended X-ray absorption fine structure (EXAFS) fitting of the synthetic samples confirms that Zn occurs in tetrahedral coordination, with two P shells at ~2.85–3.07 Å, and two higher Ca shells at ~3.71–4.02 Å. These fit results are consistent with the most favored DFT model for Zn substitution in the Ca2 site.

1. Introduction

As the main inorganic component of the hard tissues (e.g. bone and dental enamel) of vertebrates, apatite-like materials have been extensively studied. A particular focus of these studies has related to structural aspects of substitutions in hydroxylapatite (HAP)-like materials. HAP has been considered for medical applications such as bioceramics and bone graft surgery [1–3]. Modifications of HAP-like materials have also been extensively studied to enhance mechanical and physiochemical stabilities in order to improve their suitability for restoration of hard tissues such as bone and teeth [2,4]. Previous studies have shown that the flexible structure of HAP readily accommodates cationic and anionic substitutions. This accounts for the heterogeneous compositions often found in apatite and similar phosphate mineral phases with lower degrees of crystallinity and non-stoichiometry relative to pure HAP [5–8]. The presence of magnesium in apatite, for instance, causes a decrease in crystallinity with increasing Mg content [9,10]. The incorporation of carbonate in HAP and HAP-like minerals has a considerable influence on the mechanical and physicochemical properties of the crystals and significantly affects their reactivity and solubility [4,11]. These observations demonstrate that an understanding of how trace elements are accommodated in the HAP structure is essential for evaluating and predicting its long-term stability as well as the bioavailability of incorporated trace elements.

Zn substitution in HAP has been the focus of particular interest because of its presence in all biological tissues and its diverse roles in biological functions, such as enzyme activity, nucleic acid metabolism, maintenance of membrane structure and function, hormonal activity, as well as biomineralization [12] and potentially pathological calcification [13,14]. The uptake and release of Zn in the body are strongly mediated by the bone reservoir, even though it only contains a small portion of the total body Zn [15]. Teeth have also been found to contain a significant amount of Zn, which has been used as an indicator of environmental exposure [16]. It has been recently demonstrated that Zn incorporation into implants may promote bone formation around the material [17,18].

Despite the importance of Zn interaction and storage in biological tissues and minerals, the mode of Zn incorporation in HAP, specifically the binding site and its local structure, is still not clearly understood. One reason for this uncertainty is the presence of two structurally distinct cation sites, Ca1 and Ca2, in HAP that appear to be suitable for Zn substitution. Additional uncertainty arises due to the different coordination environments that Zn can adopt, both tetrahedral and octahedral. Very few experimental studies have addressed the structure of Zn in biological apatite specimens [19–21]. Barrea et al. [19,20] used extended X-ray absorption fine structure (EXAFS) spectroscopy to examine the

* Corresponding author. Tel.: +82 2 3290 3181; fax: +82 2 3290 3189.
E-mail address: youngjlee@korea.ac.kr (Y.J. Lee).
[1] Present address: School of Engineering and Applied Sciences, Harvard University, 40 Oxford St., Cambridge, MA 02138, USA.

0142-9612/$ – see front matter © 2009 Elsevier Ltd. All rights reserved.
doi:10.1016/j.biomaterials.2009.01.043

first-shell coordination of Zn in human dental calculi. In supragingival samples they found that Zn occurs in tetrahedral coordination, which they interpreted as Zn sorbed on the apatite surface, whereas Zn in the sub-gingival samples was found to be octahedrally coordinated, which they suggested was an incorporated species. Takatsuka et al. [21] compared the Zn XANES and EXAFS data on dentine treated with Zn compounds, and found similarities between the dentine sample and a synthetic Zn-doped HAP sample. However, no detailed structural information was provided. The substitution of Zn in HAP has also been the focus of recent theoretical studies [22–24], which have suggested that Zn substitution is energetically favored in the Ca2 site over the Ca1 site.

In the present study, we systematically examine the local structure of Zn incorporated into HAP at low concentrations by combining experimental and spectroscopic results with density functional theory calculations. Our findings reveal that Zn substitution in the HAP structure is most favorable for Zn occurring in tetrahedral coordination and at the Ca2 site, with significant local structural distortion.

2. Materials and methods

2.1. Reagents and synthesis method

Three Zn-doped HAP samples were synthesized by a constant-addition method modified from Nelson and Featherstone [25]. Briefly, 50 mL of 0.21 M $Ca(NO_3)_2$, with 0.1 M KNO_3 as background electrolyte, were added by a syringe pump at a rate of 0.25 mL/min into 50 mL of 0.21 M KH_2PO_4 with 0.1 M KNO_3. At the same time, 10 mL of $ZnCl_2$ stock solution was added into the reaction vessel through a separate syringe at a rate of 50 μL/min. Three different $ZnCl_2$ concentrations were used for the stock solution: 0.25, 0.5 and 1 mM. Temperature was maintained at 75–80 °C throughout the experiment. pH of the reacting suspension was maintained by an auto titrator at 10.0 ± 0.05 using 2 N KOH with constant stirring using a Teflon stir bar. Atmospheric CO_2 was not excluded from the reaction vessel. However, due to the high temperature during our synthesis, it is unlikely that any significant amount of CO_2 dissolved into the solution. In fact, the total inorganic carbonate content in the solution was measured using the procedure described by Hall and Aller [26], and was found to be below the detection limit of ~0.2 mM.

At the end of each experiment, all suspensions were filtered using 0.22 μm polypropylene membrane filters, washed repeatedly with deionized water and dried at 60 °C. Dried powders were ground and characterized by X-ray diffraction (XRD) to confirm the formation of single-phase hydroxylapatite. A portion of the powder was digested in nitric acid and analyzed for Zn concentration by directly coupled plasma-atomic emission spectrometry (DCP-AES). These three samples were labeled according to the Zn concentration in the final product: Zn203 ppm, Zn412 ppm and Zn883 ppm, with corresponding initial $ZnCl_2$ syringe concentrations of 0.25, 0.5 and 1 mM.

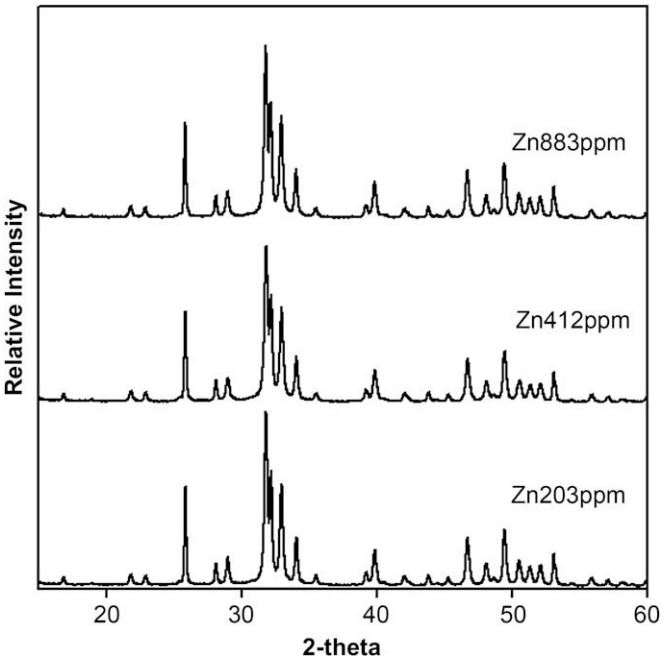

Fig. 1. X-ray diffractograms of synthetic Zn-doped HAP samples. CuKα radiation.

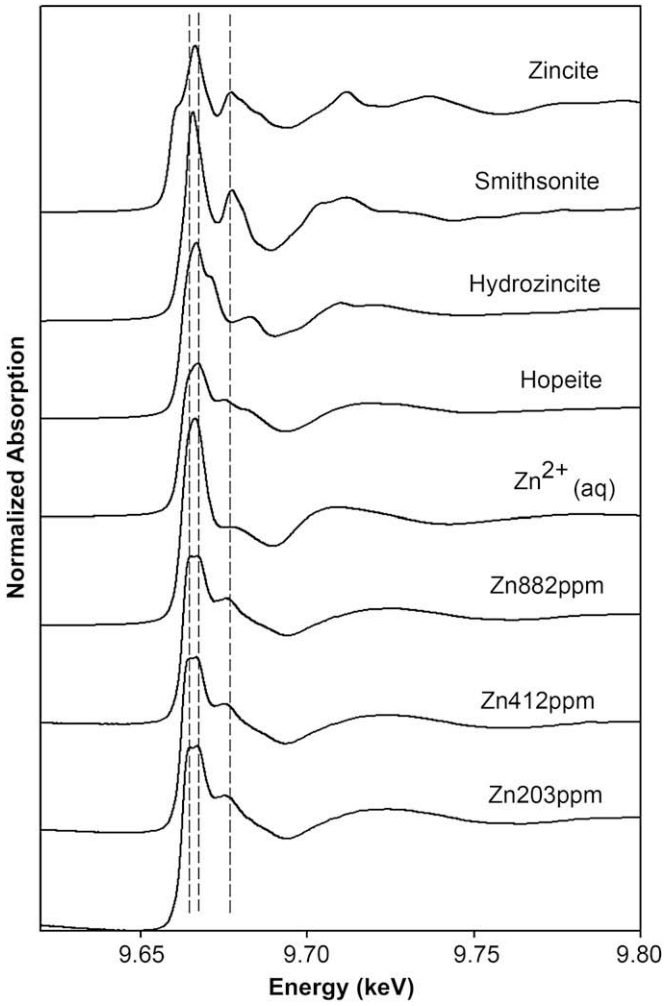

Fig. 2. Normalized Zn K-edge XANES spectra of Zn model compounds and three Zn-doped HAP samples.

Because of the rapid incorporation of Zn into the HAP precipitate, it is difficult to evaluate saturation states with respect to other Zn-containing phases. Aliquots of the reacting suspension were taken periodically over the duration of the experiments for Zn solution concentration analysis (after filtration), and were found to be at or below the detection limit of ~50 ppb by DCP, which confirm that Zn is effectively scavenged from the solution by co-precipitation with HAP. Nevertheless, for speciation calculations we used 1 μM (~60 ppb) Zn solution concentration as being representative of aqueous speciation. Saturation indexes (S.I., defined as $\log(Q/K_{eq})$) calculated using the program PHREEQC [27] at experimental conditions with 1 μM Zn^{2+} and 0.2 mM total CO_3^{2-} indicate that the solution is undersaturated with respect to all Zn-carbonates (i.e., smithsonite and hydrozincite), Zn-phosphates (i.e., hopeite), and $Zn(OH)_2$, and is only slightly oversaturated with respect to zincite (S.I. = 0.18). The latter phase is not expected to form at the conditions of these experiments.

2.2. Model compounds

Several relevant Zn-containing solids were used as model compounds for X-ray absorption spectroscopy (XAS) analysis, including reagent grade ZnO (zincite), $ZnCO_3$ (smithsonite), $Zn_5(CO_3)_2(OH)_6$ (natural hydrozincite, from the Smithsonian Institution), 50 mM $ZnCl_2$ solution, and $Zn_3(PO_4)_2{\cdot}4H_2O$ (hopeite). Hopeite was synthesized at room temperature and 50 °C using the method described by Pawling and Trettin [28]. An XRD pattern of the solid product was consistent with that reported for α-hopeite [28].

2.3. X-ray absorption spectroscopy analysis

Zn K-edge extended X-ray absorption fine structure (EXAFS) spectra were collected on the Zn-doped samples and model compounds at sector 20-BM (operated by PNC-CAT) at the Advanced Photon Source (APS; Argonne National Laboratory, Argonne, IL) and at beamline X18B of the National Synchrotron Light Source (NSLS; Brookhaven National Laboratory, Upton, NY). Data for the Zn-doped HAP samples were collected in fluorescence mode with samples mounted in a Lucite sample holder covered with Kapton tape and placed at 45° to the incident beam. Fluorescence data were collected using a Canberra 13-element Ge solid-state detector. Data for the model compounds were collected at room temperature in transmission mode. Materials were mixed with a calculated amount of BN and sealed in aluminum sample holders, which were then placed at 90° to the incident beam. Energy calibration used a Zn metal foil (K-edge 9659 eV). In order to minimize third-order harmonics, a harmonic rejection mirror was used, combined with 10% detuning of the Si(111) crystal, at sector 20-BM (APS), whereas a detuning of 30% was used at X18B (NSLS).

Data processing was performed using the EXAFS data analysis programs WinXAS [29] and IFEFFIT [30]. Spectra were averaged after energy calibration of individual data files. The μ_0 fitting used a cubic spline. The $\chi(k)$ function was Fourier transformed using k^3 weighting, and all shell-by-shell fitting was done in R-space. Theoretical backscattering paths were calculated using FEFF7 [31]. A single threshold energy value (ΔE_0) was allowed to vary during fitting. The amplitude reduction factor, S_0^2, was determined from fits of the model compounds and was fixed at $S_0^2 = 1$ for unknown samples. Due to the large correlation between coordination number (CN) and Debye–Waller (DW) factor, CN values for zincite and smithsonite were fixed to their known values. For unknown samples (Zn-doped HAP), DW factors were fixed at representative values when multiple close-by shells are present, especially when at high distances and/or involving weak backscattering atoms such as P. Errors for the fitting parameters are estimated from fits of the model compounds. Error estimates are ±0.01 Å for the R value of the first oxygen shell, and ±0.05 Å for higher distance shells. For coordination number, the estimated error is ±20% for the first oxygen shell and ±50% for shells at higher distance. Estimated errors for the Debye–Waller factors are ±0.001 Å^2 for the first-shell and ±0.005 Å^2 for higher shells.

3. Results and discussion

3.1. X-ray diffraction analysis

XRD patterns of the three synthetic HAP samples were obtained on a Scintag PADx diffractometer with Cu Kα radiation ($\lambda = \sim 1.5415$ Å) and a solid-state Ge detector. Intensity data were collected over the range of 15–60° 2θ. All three synthetic samples show well-resolved diffraction patterns consistent with pure HAP (Fig. 1). No peaks indicating the presence of other phases were observed. However, given the small amounts of incorporated Zn, the XRD results cannot rule out the possible existence of minor amounts of Zn-containing impurity phases.

Although Zn has been shown to inhibit the growth of HAP, systematic incorporation and co-precipitation studies [32,33] have shown that considerable amounts of Zn can be incorporated into HAP. Miyaji et al. [33] studied progressive Zn substitution in HAP and their findings indicate that, for increasing Zn concentration, the final product changes from Zn-substituted apatite to amorphous

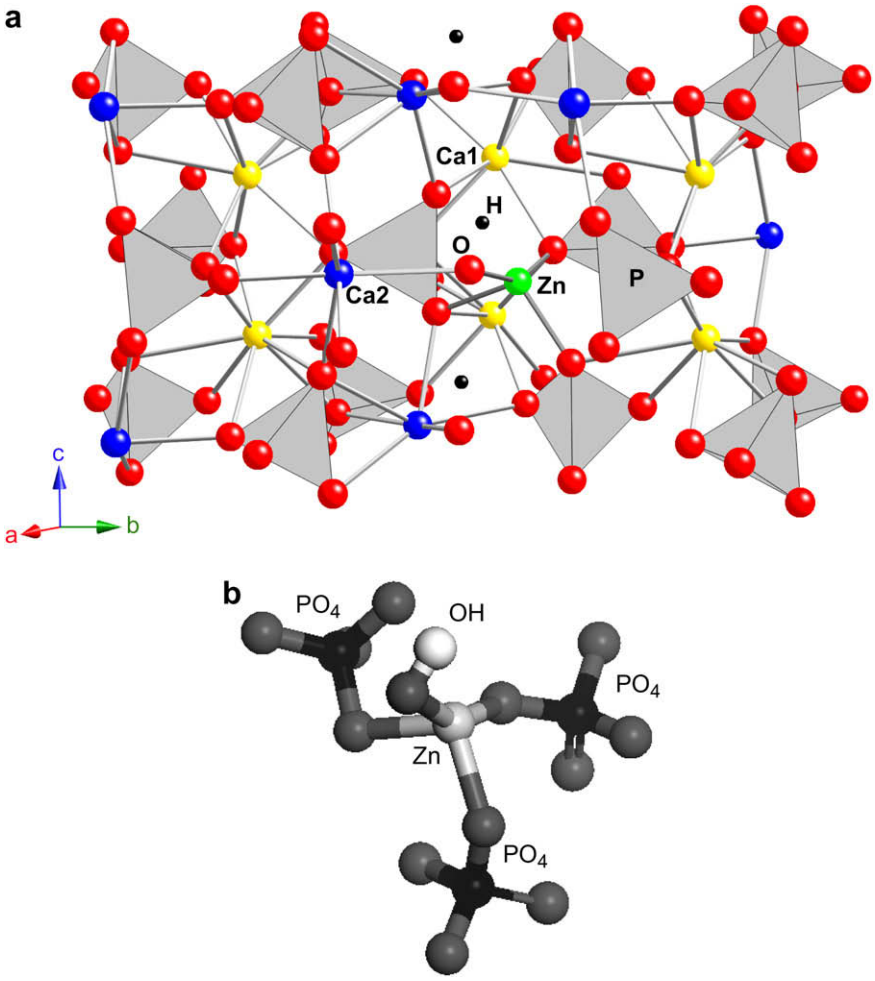

Fig. 3. (a) Optimized structure of Zn-doped HAP. Ca1 site, Ca2 site, O, H and Zn atoms are shown as yellow, blue, red, black and green spheres, respectively. Phosphate groups are shown as grey tetrahedra; (b) detailed view of the local coordination of Zn incorporated in HAP structure.

apatite-like phase and then to amorphous + parascholzite ($CaZn_2(PO_4)_2 \cdot 2H_2O$). The *c* lattice parameter of HAP was found to decrease progressively with increasing Zn concentration. They also observed an increase in the *a*-lattice parameter for higher Zn concentration, which was ascribed to increased H_2O substitution for OH. They suggested the substitution limit of Zn in HAP is 15 mol%, as compared to 25 mol% suggested by Bigi et al. [32]. Therefore the relatively low Zn concentrations in our samples are unlikely to adversely affect the crystallinity.

3.2. X-ray absorption near edge structure (XANES) spectroscopy

X-ray absorption near edge structure (XANES) data for the three synthetic samples and several Zn-containing model compounds are shown in Fig. 2. XANES spectra of all three synthetic samples are essentially identical. They all show a peak doublet for the white line feature at ~9.66 keV (as indicated by the two left-most dashed lines) and a subsidiary peak or shoulder at ~9.675 keV (indicated by the right-most dashed line). These features are very different from those observed in all the other model compounds, and no similarities were found with a single model compound. It was initially suspected that these features might result from multiple phases. However, the three synthetic samples with Zn concentrations ranging from 203 to 883 ppm show virtually identical features, which is indicative of a single coordination environment being dominant. If multiple Zn species were present, one would expect their proportions to change with different Zn concentrations, and therefore result in a change of the XANES spectra. In fact, since our selection of model compounds covered a wide range of Zn-containing materials, we conducted linear combination fits (LCF) using combinations of these model compounds as end members, and could not obtain reasonable fits. Inasmuch as XANES is very sensitive to the change of local coordination environments, the overall similarities among the XANES spectra of samples are suggestive of similar Zn coordination environment.

It has been shown that the relative intensity of the white line feature in Zn K-edge XANES can be used to distinguish between tetrahedral and octahedral coordination environments [34]. Smithsonite and $Zn^{2+}_{(aq)}$ XANES both show a prominent white line intensity in comparison to the other model compounds, which is usually observed for Zn in octahedral coordination. The suppressed white line observed in zincite and all the Zn-doped HAP samples is characteristic of Zn in a tetrahedral coordination environment [34,35]. Both hydrozincite and hopeite have Zn in mixed octahedral and tetrahedral coordination with a ratio of oct:tet = 3:2 and 1:2, respectively [36,37]. Because hydrozincite has a higher oct:tet ratio than hopeite, its white line is slightly more prominent than that in the spectrum of hopeite.

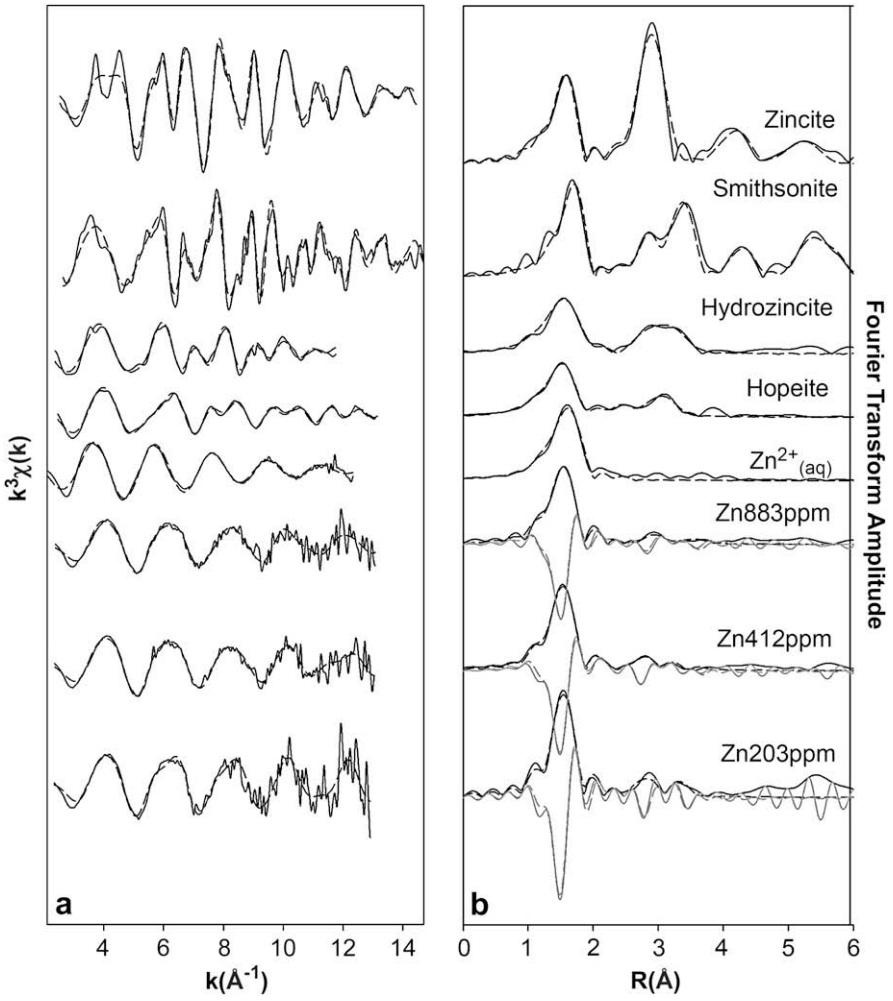

Fig. 4. (a) The k^3-weighted EXAFS data (solid lines) and best fits (dashed lines) for Zn-doped HAP and reference compounds; (b) corresponding Fourier transform amplitudes (black solid lines) and best fits in R-space (black dashed lines). Imaginary component and fit are shown in gray solid and dashed lines for the Zn–HAP spectra. Fourier transforms are not corrected for phase shifts.

3.3. Density function theory (DFT) calculation

In order to predict the most stable coordination environment of Zn in HAP, a series of calculations were undertaken, substituting Zn into the HAP unit cell. The CASTEP density function theory (DFT) code [38] was used. A kinetic cut-off energy of 400 eV was employed and a *k*-point grid of $3 \times 3 \times 4$ was used to sample the Brillouin zone [39]. The generalized gradient-approximation (GGA) and the PBE exchange-correlation potential were used throughout [40]. The convergence thresholds between geometry optimization cycles for energy change, maximum force, maximum stress and maximum displacement were set to 0.1×10^{-4} eV atom^{-1}, 0.05 eV Å^{-1}, 0.05 GPa and 0.001 Å, respectively. The phase-pure hexagonal unit cell (obtained from the Materials Studio package (Accelrys)) contains 44 atoms and after relaxation the cell parameters were found to be $a = b = 9.488$ Å and $c = 6.849$ Å. These values agree to within 1% of experimental values [41]. In the geometry optimized cell there are 10 possible Ca positions for Zn substitution: four Ca1 positions and six Ca2 positions. It is relevant to initially look at all 10 sites, as it is not guaranteed that all Ca1 and all Ca2 positions will be of the same energy, even though we would expect all positions of the same kind to be identical. In this way, the range of values that are obtained for all positions of one kind gives an error value for the calculations. Substitution into the P position was not considered as our initial EXAFS fitting, because substitution in this site is very unlikely (as described in Section 3.4). In addition, a previous experimental study [42] showed that the (Ca + Zn)/P ratio remained at the phase-pure HAP value of 1.67, confirming Ca positions as the substitution sites. In order to determine the most stable configuration, formation energies were calculated using,

$$E_f = E_{ZnHA} - (E_{HA} - \mu_{Ca} + \mu_{Zn})$$

where E_{ZnHA} is the energy of a unit cell containing a Zn substitution and E_{HA} is the energy of an optimized unit cell with no substitutions. μ_{Ca} and μ_{Zn} are the chemical potentials of Ca and Zn ions, respectively. These were calculated as previously described [43], by approximating the 0 K energies per atom or molecule. The choice of suitable sources depends on the range of commonly occurring oxides and the potentials chosen were those from the lowest energy materials, which were, in this case, metallic Zn and metallic Ca, respectively. The same chemical potential sources were also chosen in the recently published study on Zn and Mg substitutions [24].

In terms of formation energies, among all 10 possible positions, Zn substitution in the Ca2 site was always found to be preferred, with the lowest formation energy (4.636 eV), 6.2% lower than the highest formation energy (4.940 eV) for Zn in the Ca1 site. In fact, the lowest formation energy in a Ca1 (4.771 eV) site is still 3% higher than the best Ca2 position. All the Ca2 positions are lower in energy than the Ca1 positions and the range of values among the Ca2 positions is just 0.013 eV. This is small and equates to all Ca2 positions being of approximately the same energy cost, as would be expected, with an error of approximately 0.01 eV. These calculations unequivocally show that substitution in the Ca2 position is energetically favored. This result agrees with the study by Terra et al. [22], which employed an embedded cluster LCAO method, and Matsunaga [24], who used the projector augmented wave method. Both concluded that Zn energetically prefers the Ca2 site. Additionally, Ma and Ellis [23] suggest that the Ca2 site is to be favored for Zn substitution at the HAP (0001) surface. Both Terra et al. [22] and Ma and Ellis [23] suggested Zn to be octahedrally coordinated. Our calculations show that the most favorable structure (with the lowest formation energy) has Zn in tetrahedral coordination, as shown in Fig. 3, and is consistent with the result of Matsugana [24]. Our results show that all Ca2 sites allow the Zn in 4-fold (tetrahedral) coordination, whereas the Ca1 sites, which we already showed to be unfavorable through the formation energy analysis, have a mixture of 5- and 6-fold coordination.

Looking more closely at the most favorable structure, Fig. 3 shows that among the four oxygen atoms bonded to Zn, one is from the nearest hydroxyl group and three are from the adjacent phosphate (PO_4) groups. Such arrangement of atoms accounts for a reduction in the *a*-lattice parameter of this cell from 9.488 to 9.319 Å, as the hydroxyl group moves off its *c*-axis position and toward the Zn atom, and the Zn atom moves off the Ca2 site toward the hydroxyl group. The Zn–O(OH) distance is 2.02 Å and the Zn–H(OH) distance is 2.30 Å, as compared to the ideal distances in HAP of 2.69 Å and 2.38 Å, respectively. Ma and Ellis [23] and Matsugana [24] have also observed similar shifts of the Zn atom and hydroxyl group toward each other. Further electronic structure and bonding analysis of the unit cell from our modeling results, which are not relevant to this study, are presented in another publication [44].

3.4. Extended X-ray absorption fine structure (EXAFS)

The k^3-weighted raw and fitted Zn K-edge EXAFS data for the model compounds are shown in Fig. 4, with fit results shown in Table 1. The fitted first-shell Zn–O distances of smithsonite (~2.10 Å) and $Zn^{2+}_{(aq)}$ (~2.08 Å) are typical for Zn in octahedral coordination, in agreement with their known structures, and are noticeably longer than the Zn–O distances obtained from fits of the other model compounds, which contain Zn in tetrahedral coordination or a mixture of tetrahedral and octahedral coordination. Zincite has a first-shell Zn–O distance of 1.97 ± 0.01 Å, in agreement with its known structure [45]. Hydrozincite contains two similar octahedral Zn sites and one tetrahedral Zn site, with a ratio of 3:2 [36]; therefore the weighted average Zn–O distance is ~2.04 Å, in agreement with our EXAFS fitting results of ~5.7 O at ~2.03 Å. Hopeite contains tetrahedral and octahedral Zn sites in a ratio of 2:1 [37]; our EXAFS fitting results show ~4.7 O at ~1.98 Å, similar

Table 1
EXAFS fitting results of Zn model compounds.

Shell	CN	*R* (Å)	σ^2 (Å^2)	E_0(eV)	R^a (%)
ZnO (Zincite)					
Zn–O	4[b]	1.97	0.004	1.23	17.1
Zn–Zn	12[b]	3.22	0.009		
Zn–Zn	12[b]	4.56	0.011		
Zn–Zn	2[b]	5.18	0.014		
Zn–Zn	18[b]	5.63	0.012		
$ZnCO_3$ (Smithsonite)					
Zn–O	6[b]	2.10	0.005	6.75	14.8
Zn–C	6[b]	2.99	0.006		
Zn–O	6[b]	3.22	0.005		
Zn–Zn	6[b]	3.67	0.006		
Zn–Zn	6[b]	4.64	0.007		
Zn–Zn	6[b]	5.64	0.004		
Zn–Zn	5[b]	5.99	0.002		
$Zn_5(CO_3)_2(OH)_6$ (Hydrozincite)					
Zn–O	5.7	2.03	0.013	−0.28	7.8
Zn–Zn	1.7	3.14	0.01[b]		
Zn–Zn	2.4	3.55	0.007		
$Zn_3(PO_4)_2{\cdot}4H_2O$ (Hopeite)					
Zn–O	4.7	1.98	0.011	1.92	7.6
Zn–P	1.1	3.10	0.008		
Zn–Zn	0.9	3.37	0.003		
Zn^{2+} (aq)					
Zn–O	6.2	2.08	0.009	−0.11	9.44

[a] Residual(%) $= \sum_{i=1}^{N} |y_{exp}(i) - y_{theo}(i)| / \sum_{i=1}^{N} |y_{exp}(i)| \times 100$, with N the number of data points, y_{exp} and y_{theo} experimental and theoretical data points, respectively.
[b] Fixed value.

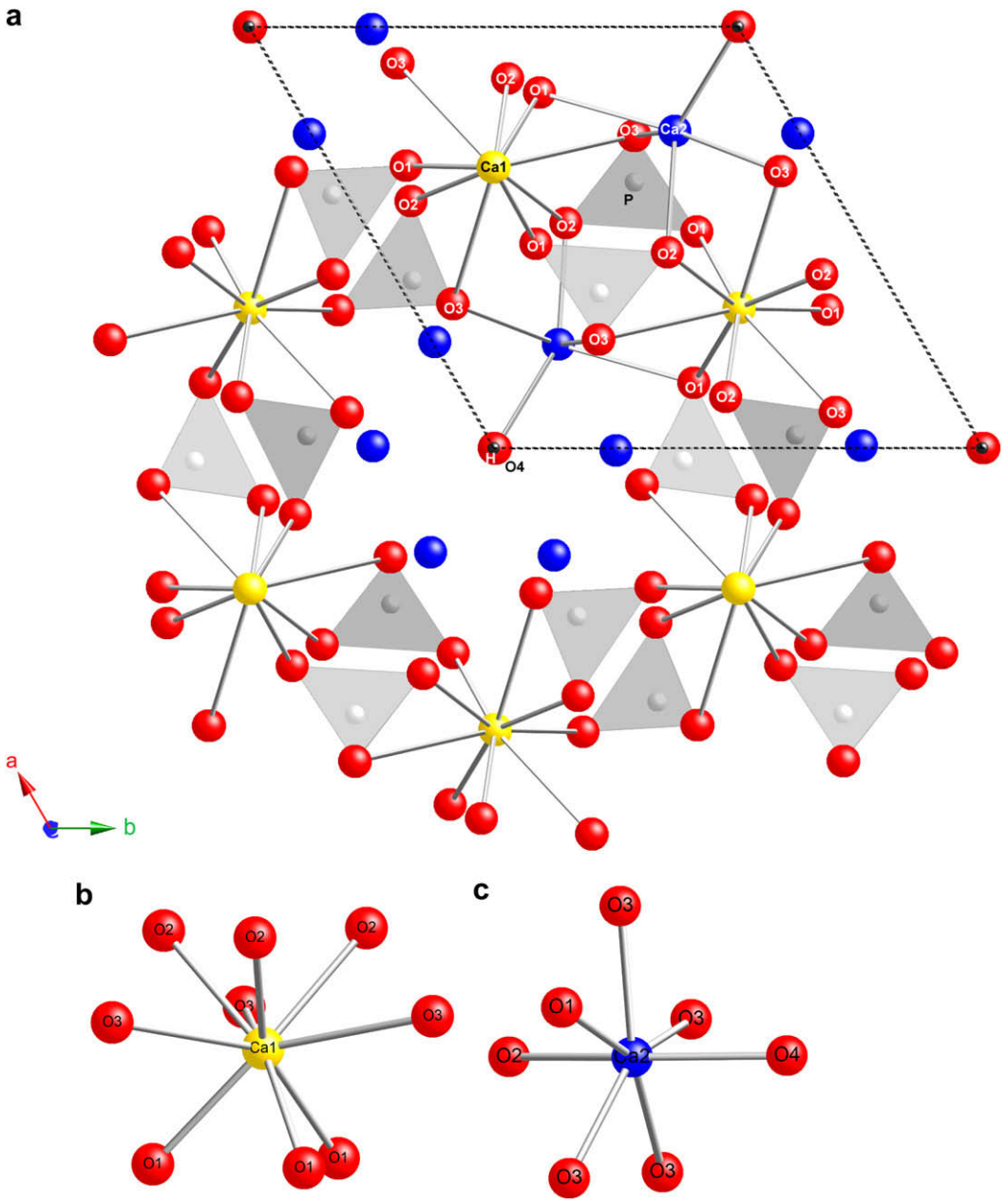

Fig. 5. (a) HAP structure viewed along the *c*-axis. Also shown are the structural configurations of (b) the Ca1 and (c) Ca2 sites. Ca1, Ca2, O and H atoms are shown as red, blue, yellow and black spheres, respectively. Phosphate groups are shown as gray tetrahedra.

to the weighted average Zn–O coordination number and distance of ~4.8 O at ~2.03 Å.

There are three sites in HAP that Zn could possibly occupy, the Ca1, Ca2 and P sites (Fig. 5). These sites are distinctively different from each other in terms of their local coordination environments. Based on the structure model of Hughes et al. [46], backscattering paths calculated for the Ca1, Ca2 and P sites in pure HAP are shown in Table 2. The Ca1 site is 9-coordinated with O atoms at ~2.40–2.80 Å, and the higher shells consists of 3 P at ~3.21 Å, 2 Ca at ~3.43 Å, 3 P at ~3.59 Å and 6 Ca at ~3.94–4.02 Å. The Ca2 site is generally considered 7-coordinated with 6 O atoms and 1 column anion (F, OH or Cl), which is the O atom from channel hydroxyl group in our case. These O atoms are distributed at ~2.34–2.71 Å, and the higher shells consist of 1 P at ~3.08 Å, 1 P at ~3.29 Å, 1 P at ~3.46 Å, 2 P at ~3.66 Å, 6 Ca at ~3.94–4.08 Å, and 4 Ca at ~4.17 Å. The P site is the center of PO_4 tetrahedra with P–O distances of ~1.53 Å. As suggested by XANES and DFT results, the incorporated Zn in HAP is likely to be tetrahedrally coordinated, therefore raising the possibility of it occupying the P site in HAP. However, due to the charge difference (Zn^{2+} vs. P^{5+}) and the size difference (0.74 Å vs. 0.31 Å for tetrahedrally coordinated Zn^{2+} and P^{5+}, respectively) [47], it is very unlikely for Zn to substitute at the P site, which would disturb both the local structure and charge balance. We consider Ca1 and Ca2 sites to be more suitable for Zn substitution as both contain divalent cations. In fact, a previous experimental study [42] showed that the (Ca + Zn)/P ratio remains at 1.67, the value of phase-pure HAP, suggesting substitution into the calcium rather than the phosphorus sites.

Another possibility is that Zn incorporates in mixed coordination environments, or occupies intrinsic defect sites in HAP. If either of these were the cases, then one would expect the averaged XAS signal to be different with different Zn concentration. However, our

Table 2
Local interatomic distances calculated for Ca1, Ca2 and P sites in pure HAP based on the structure model of Hughes et al. [46].

Ca1 site			Ca2 site			P site		
Shell	CN	R (Å)	Shell	CN	R (Å)	Shell	CN	R (Å)
Ca1–O1	3	2.403	Ca2–O4	1	2.343	P–O3	2	1.530
Ca1–O2	3	2.452	Ca2–O2	1	2.353	P–O1	1	1.534
Ca1–O3	3	2.801	Ca2–O3	2	2.385	P–O2	1	1.537
Ca1–P	3	3.210	Ca2–O3	2	2.509	P–Ca2	1	3.078
Ca1–Ca1	1	3.417	Ca2–O1	1	2.711	P–Ca1	2	3.210
Ca1–Ca1	1	3.457	Ca2–P	1	3.078	P–Ca2	1	3.287
Ca1–P	3	3.592	Ca2–P	1	3.287	P–Ca2	1	3.460
Ca1–Ca2	3	3.943	Ca2–P	1	3.460	P–Ca1	2	3.592
Ca1–Ca2	3	4.025	Ca2–P	2	3.664	P–Ca2	2	3.664
			Ca2–Ca1	2	3.943			
			Ca2–Ca2	2	4.025			
			Ca2–Ca1	2	4.084			

XANES observations show one dominant coordination environment over a range of Zn concentrations.

In order to determine the substitution site and further characterize the local environment of Zn incorporated in HAP, two approaches were taken for analyzing the EXAFS spectra. The first approach used backscattering paths calculated using initial models of Zn in the Ca1, Ca2 or P site of HAP (Table 2). Although the P site is not likely for Zn substitution, we nevertheless attempted EXAFS analysis using this model. Regardless of the starting model, the first coordination shell is always best fit with ~4 O atoms at $\sim 1.96 \pm 0.01$ Å, confirming Zn coordination in a tetrahedral unit, consistent with our XANES and DFT results. Comparing this Zn–O distance to the first-shell Ca1–O, Ca2–O and P–O distance shown in Table 2, there is a clear mismatch with respect to the structure. Therefore our expectation is that Zn occupancy in the Ca1 or Ca2 site would cause shrinkage of the local structure, whereas an expansion would be needed for Zn occupancy in the P site. Fits were performed using the initial parameters calculated for each of the three sites, and fixing the coordination numbers of higher shells. For the fits with Zn in the Ca1 site and in the P site, all the higher shells move to longer and shorter distances, respectively, relative to starting values, which contradicts our expectation. Fits for Zn in Ca2 site result in overall shrinkage of the local structure, with most of the higher shells moving closer to Zn.

However, as shown in Table 2, there are several higher shells around the Ca2 site that complicate EXAFS fits, suggesting that a fit with better structure configuration is needed. Therefore we adopted a second approach using the optimized structure model from DFT calculation. Atomic positions derived from the optimized structure of Zn at the Ca2 site in tetrahedral coordination (Fig. 3) were used to calculate X-ray backscattering paths around the central Zn atom (Table 3). Zn is bonded to three phosphate oxygens and a hydroxyl oxygen with Zn–O distances of 1.99–2.09 Å. There are three Zn–P distances between 2.85 and 3.36 Å, and several Zn–Ca shells at higher distances. Using these scattering paths as an initial model, EXAFS fitting results were obtained for all the Zn–HAP samples (Fig. 4 and Table 4). Fig. 4 shows the raw and fitted data of the synthetic Zn-doped HAP. Their Fourier transforms are all dominated by the first oxygen shell backscattering at ~1.6 Å in R-space (indicated by dashed line and not corrected for phase shifts), similar to that of the model compounds containing tetrahedrally coordinated Zn. This peak is best fit with ~4 oxygen atoms at $\sim 1.96 \pm 0.01$ Å, consistent with Zn–O distance as determined by EXAFS for tetrahedral coordination of Zn [35,48–51], and in agreement with our previous XANES observation. For higher shell contributions shown in the Fourier transforms of synthetic Zn–HAP samples, especially the features at ~2.5–3.5 Å, best fit results were obtained by the combination of two P shells at ~2.82 and 3.03 ± 0.05 Å, and two higher Ca shells at ~3.76 and 3.95 ± 0.05 Å.

Table 3
Backscattering paths calculated from the optimized DFT model for Zn substitution in the Ca2 site of HAP.

Shell	CN	R (Å)	Shell	CN	R (Å)
Zn–O	1	1.990	Zn–P	1	3.363
Zn–O	1	2.022	Zn–Ca	1	3.636
Zn–O	1	2.064	Zn–Ca	1	3.700
Zn–O	1	2.087	Zn–P	1	3.797
Zn–O	1	2.581	Zn–Ca	1	3.916
Zn–P	1	2.848	Zn–Ca	1	3.967
Zn–O	1	2.982	Zn–Ca	1	4.030
Zn–P	1	3.197	Zn–Ca	1	4.044

By comparing the Zn EXAFS fitting results with the coordination environments of the Ca1 and Ca2 sites, it is evident that the overall distributions of P and Ca atoms are similar to those of the Ca2 site, with ~1 P at $\sim 2.82 \pm 0.05$ Å, ~1–2 P at $\sim 3.03 \pm 0.05$ Å, ~2–3 Ca at $\sim 3.76 \pm 0.05$ Å and ~1–4 Ca at $\sim 3.95 \pm 0.05$ Å. Considering the large difference between the ZnO_4 tetrahedron with $\langle Zn–O \rangle = \sim 1.96$ Å and the CaO_7 polyhedron at Ca2 site with $\langle Ca–O \rangle = \sim 2.231–2.814$ Å, significant distortions in the local structure must exist to accommodate Zn at this site. The shorter overall radial distances from Zn in the EXAFS fitting as compared to those in the ideal HAP structure are consistent with shrinkage of the local structure around the smaller Zn atom. This is in agreement with our DFT model results showing a clear shrinkage of the Zn polyhedron as well as the results of Matsunage [24].

3.5. Possible mechanism(s) of Zn substitution in HAP

We demonstrated that Zn incorporates into the Ca2 site of HAP in tetrahedral coordination, with significant local structural distortion (i.e., shrinkage around the Zn dopant). DFT modeling and the overall similarities of XAS results among samples of different Zn concentration also suggest such substitution as the dominant and favored mode. However, several questions still remain. Although DFT results suggest the Ca2 site is energetically favored over the Ca1 site, substitution of Ca by Zn at both sites is endothermic, i.e., energetically unfavorable. Theoretical studies by Matsunaga [24] and Ma and Ellis [23] showed similar endothermic behaviors for Zn substitution in bulk HAP and on the (0001) surface, respectively. However, dopant incorporation is commonly kinetically controlled during irreversible processes. Our experiments are based on a co-precipitation method, where Zn is simultaneously incorporated into the HAP structure during the fast crystallization process, and is more representative of a kinetic effect rather than a bulk thermodynamic effect. It is most likely that Zn directly substitutes at Ca sites during this process, and remains trapped as defect sites.

As for the site preference of metal ions in the HAP structure, despite considerable research there is still debate concerning how metal ions choose between the Ca1 and Ca2 sites. Several factors have been proposed for determining site preferences, such as substitution mechanisms, equalization of bond valence and spatial accommodation [52]. As shown in Fig. 5(a), the linkage of Ca1 polyhedra and PO_4 tetrahedra forms a framework that defines tunnels, which contain the Ca2 sites and the exchangeable channel anion sites. So, the fact that Zn shows a strong preference for the Ca2 site may mean that it can be incorporated into the structure more readily without disrupting the framework. Fig. 5(b) and (c) shows the local binding configuration of Ca1 and Ca2 sites. The Ca1 site is coordinated to six near oxygen atoms, three O1 and three O2 atoms in planes 1/2 unit cell above and below Ca1, forming meta-prisms that compose the ring-like Ca1–PO_4 framework. Ca1

Table 4
EXAFS fitting results of Zn–HAP samples using the optimized DFT model.

Shell	CN	R (Å)	σ^2 (Å^2)	E_0 (eV)	R^a (%)
Zn203ppm					
Zn–O	3.4	1.95	0.002	−0.50	14.9
Zn–P	1.2	2.85	0.005[b]		
Zn–P	1.9	3.06	0.005[b]		
Zn–Ca	3.0	3.82	0.01[b]		
Zn–Ca	0.6	4.02	0.01[b]		
Zn412ppm					
Zn–O	4.4	1.96	0.005	−0.53	7.3
Zn–P	0.9	2.79	0.002		
Zn–P	1.4	3.01	0.005		
Zn–Ca	1.6	3.72	0.01[b]		
Zn–Ca	4.0	3.90	0.019		
Zn883ppm					
Zn–O	3.5	1.95	0.005	−0.51	11.4
Zn–P	1.2	2.85	0.008[b]		
Zn–P	1.1	3.07	0.007		
Zn–Ca	2.0	3.71	0.01[b]		
Zn–Ca	1.7	3.90	0.007		

[a] Residual (%).
[b] Fixed value.

coordinates to three more distant O3 atoms through the prism faces to form a tricapped trigonal prism [7]. Each $Ca1O_9$ polyhedron shares faces with the $Ca1O_9$ polyhedra above and below. The Ca2 site is bonded to 6 oxygen atoms (O1, O2 and four O3 atoms) and one column anion (O4 from hydroxyl group in our case). Two of the O3 atoms are from one phosphate group. Therefore the CaO_7 polyhedron is connected with surrounding phosphate and hydroxyl groups via sharing of five corners and one edge. Our DFT results show that Zn occupation at the Ca1 site, although energetically unfavorable, prefers 5- or 6-fold coordination, whereas Zn at the Ca1 site prefers 4-fold (tetrahedral) coordination. As we discussed before, the Zn–O distances in octahedral and tetrahedral coordination are ~2.08–2.10 Å and ~1.96–1.98 Å, respectively, both significantly shorter than the Ca–O distances in the Ca2 (~2.34–2.71 Å) and Ca1 (2.40–2.80 Å) sites. Regardless of which coordination Zn possesses at either site, the local environment must distort in order to accommodate such a substitution; for example, an overall shrinkage as suggested by the EXAFS results for Zn substitution at the Ca2 site. If Zn was to occupy the Ca1 site, it would disrupt the face-sharing with $Ca1O_9$ polyhedra below and above, essentially interrupting the Ca1–PO_4 framework and potentially collapsing the tunnels. On the other hand, when Zn occupies the Ca2 site, the local shrinkage, which causes the ZnO_4 tetrahedron and the channel hydroxyl groups to move closer together, minimizes the effect on adjacent Ca1 sites and avoids any disruption of the framework.

4. Conclusions

By combining X-ray absorption spectroscopy analysis and density function theory calculation, we examined the mechanism(s) for Zn incorporation in the hydroxylapatite structure. Both XANES and DFT results suggest tetrahedral coordination for Zn and one dominant coordination environment. DFT calculations also show that Zn prefers the Ca2 site over the Ca1 site, with the channel hydroxyl group and Zn moving toward each other and an overall shrinkage of the local structure. EXAFS fitting results agree with XANES and DFT results that Zn occurs in tetrahedral coordination, with two P shells at ~2.85–3.07 Å, and two higher Ca shells at ~3.71–4.02 Å, consistent with Zn substitution at Ca2 site with an overall shrinkage of the local environment. This study of the structural behavior of Zn in synthetic HAP provides valuable information for future studies of Zn storage and transport involving calcified hard tissues and therefore the regulation of Zn metabolism in the body. However, biological apatite materials are known to be different from pure HAP in that they usually contain other impurities, especially high concentrations of carbonate (up to ~8%) groups [53] and may be Ca deficient. The factors controlling different modes of carbonate incorporation into biological apatite are still being investigated, and may influence the Zn coordination environment. And of course, the actual crystallites in bone and teeth are generally considered nano-crystalline, so the exposure of sites is also an important factor. Nevertheless, the preference of Zn for the Ca2 site may facilitate uptake and release of Zn by biological HAP because it would not disrupt the framework of the structure.

Acknowledgement

YT and RJR were supported by Center for Environmental Molecular Science through NSF grant CHE-0221924. HFC and MTD acknowledge the support from NERC, UK. YJL was supported by the Korean Research Foundation Grant funded by the Korean Government (KRF-2007-331-C00250). Use of the National Synchrotron Light Source and Advanced Photon Source was supported by the U.S. Department of Energy, Office of Science, Office of Basic Energy Sciences, under Contract No. DE-AC02-98CH10886 and DE-AC02-06CH11357, respectively.

Appendix

Figures with essential colour discrimination. Parts of Figures 3 and 5 in this article may be difficult to interpret in black and white. The full colour images can be found in the on-line version, at doi:10.1016/j.biomaterials.2009.01.043.

References

[1] Hench LL, Wilson J. An introduction to bioceramics. Singapore: World Scientific; 1993.
[2] Glimcher MJ. Bone: nature of the calcium phosphate crystals and cellular, structural, and physical chemical mechanisms in their formation. In: Sahai N, Schoonen MAA, editors. Medical mineralogy and geochemistry. Reviews in mineralogy and geochemistry, vol. 64. Washington, DC: Mineralogical Society of America; 2006. p. 223–82.
[3] Hing KA, Wilson LF, Buckland T. Comparative performance of three ceramic bone graft substitutes. Spine J 2007;7:475–90.
[4] Elliott JC. Calcium phosphate biominerals. In: Kohn MJ, Rakovan J, Hughes JM, editors. Phosphates: geochemical, geobiological, and materials importance. Reviews in mineralogy and geochemistry, vol. 48. Washington, DC: Mineralogical Society of America; 2002. p. 427–53.
[5] Pieters IY, De Maeyer EAP, Verbeeck RMH. Stoichiometry of K^+- and CO_3^{2-}-containing apatites prepared by the hydrolysis of octacalcium phosphate. Inorg Chem 1996;35:5791–7.
[6] Kapolos J, Koutsoukos PG. Formation of calcium phosphates in aqueous solutions in the presence of carbonate ions. Langmuir 1999;15:6557–62.
[7] Hughes JM, Rakovan J. The crystal structure of apatite: $Ca_5(PO_4)_3(F, OH, Cl)$. In: Kohn M, Rakovan J, Hughes JM, editors. Phosphates: geochemical, geobiological and materials importance. Reviews in mineralogy and geochemistry, vol. 48. Washington, DC: Mineralogical Society of America; 2002. p. 1–12.
[8] Mason HE, Kozlowski A, Phillips BL. Solid-state NMR Study of the role of H and Na in AB-type carbonate hydroxylapatite. Chem Mater 2008;20:294–302.
[9] Ennever J, Vogel JJ. Magnesium inhibition of apatite nucleation by proteolipid. J Dent Res 1981;60:838–41.
[10] Okazaki M. Crystallographic behavior of fluoridated hydroxyapaptites containing magnesium and carbonate ions. Biomaterials 1991;12:831–5.
[11] Iijima M, Kamemizu H, Wakamatsu N, Goto T, Doi Y, Moriwaki Y. Effects of CO_3^{2-} ion on the formation of octacalcium phosphate at pH 7.4 and 37 °C. J Cryst Growth 1994;135:229–34.
[12] Murray EJ, Messer HH. Turnover of bone zinc during normal and accelerated bone loss in rats. J Nutr 1981;111:1641–7.
[13] Bazin D, Chevallier P, Matzen G, Jungers P, Daudon M. Heavy elements in urinary stones. Urol Res 2007;35:179–84.
[14] Bazin D, Carpentier X, Traxer O, Thiaudiere D, Somogyi A, Reguer S, et al. Very first tests on SOLEIL regarding the Zn environment in pathological calcifications made of apatite determined by X-ray absorption spectroscopy. J Synchrotron Radiat 2008;15:506–9.

[15] Windisch W. Homeostatic reactions of quantitative Zn metabolism on deficiency and subsequent repletion with Zn in Zn-65-labeled adult rats. Trace Elem Electrolytes 2001;18:122–8.
[16] Tvinnereim HM, Eide R, Riise T, Fosse G, Wesenberg GR. Zinc in primary teeth from children in Norway. Sci Total Environ 1999;226:201–12.
[17] Ito A, Kawamura H, Otsuka M, Ikeuchi M, Ohgushi H, Ishikawa K, et al. Zinc-releasing calcium phosphate for stimulating bone formation. Mater Sci Eng 2002;C22:21–5.
[18] Ito A, Ojima K, Naito H, Ichinose N, Tateishi T. Preparation, solubility, and cytocompatibility of zinc-releasing calcium phosphate ceramics. J Biomed Mater Res 2000;50:178–83.
[19] Barrea RA, Perez CA, Ramos AY. Zinc incorporation in human dental calculus. J Synchrotron Radiat 2001;8:990–2.
[20] Barrea RA, Perez CA, Ramos AY, Sanchez HJ, Grenon M. Distribution and incorporation of zinc in biological calcium phosphates. X-ray Spectrom 2003;32:387–95.
[21] Takatsuka T, Hirano J, Matsumoto H, Honma T. X-ray absorption fine structure analysis of the local environment of zinc in dentine treated with zinc compounds. Eur J Oral Sci 2005;113:180–3.
[22] Terra J, Jiang M, Ellis DE. Characterization of electronic structure and bonding in hydroxyapatite: Zn substitution for Ca. Philos Mag A 2002; 82:2357–77.
[23] Ma X, Ellis DE. Initial stages of hydration and Zn substitution/occupation on hydroxyapatite (0001) surfaces. Biomaterials 2008;29:257–65.
[24] Matsunaga K. First-principles study of substitional magnesium and zinc hydroxyapatite and octacalcium phosphate. J Chem Phys 2008; 128:245101.
[25] Nelson DGA, Featherstone JDB. Preparation, analysis, and characterization of carbonated apatites. Calcif Tissue Int 1982;34:S69–81.
[26] Hall PO, Aller RC. Rapid, small-volume, flow injection analysis for CO_2 and NH_4^+ in marine and fresh waters. Limnol Oceanogr 1992;37:1113–9.
[27] Parkhurst DL, Appelo CAJ. User's guide to PHREEQC (version 2) – a computer program for speciation, batch-reaction, one-dimensional transport, and inverse geochemical calculations. US Geol Surv Water Res Inv Rept 1999;99–4259:310.
[28] Pawling O, Trettin R. Synthesis and characterization of α-hopeite, $Zn_3(PO_4)_2 \cdot 4H_2O$. Mater Res Bull 1999;34:1959–66.
[29] Ressler T. WinXAS: a new software package not only for the analysis of energy-dispersive XAS data. J Phys IV 1997;7:269–70
[30] Newville M. IFEFFIT: interactive XAFS analysis and FEFF fitting. J Synchrotron Radiat 2001;8:322–4.
[31] Zabinsky SI, Rehr JJ, Ankudinov A, Albers RC, Eller MJ. Multiple-scattering calculations of X-ray absorption spectra. Phys Rev 1995;B52:2995–3009.
[32] Bigi A, Foresti E, Gandolfi M, Gazzano M, Roveri N. Inhibiting effect of zinc on hydroxylapatite crystallizaion. J Inorg Biochem 1995;58:49–58.
[33] Miyaji F, Kono Y, Suyama Y. Formation and structure of zinc-substituted calcium hydroxyapatite. Mater Res Bull 2005;40:209–20.
[34] Rose J, Moulin I, Masion A, Bertsch PM. X-ray absorption spectroscopy study of immobilization processes for heavy metals in calcium silicate hydrates. 2. Zinc. Langmuir 2001;17:3658–65.
[35] Waychunas GA, Fuller CC, Davis JA. Surface complexation and precipitate geometry for aqueous Zn(II) sorption on ferrihydrite I. X-ray absorption extended fine structure spectroscopy analysis. Geochim Cosmochim Acta 2002;66:1119–37.
[36] Ghose S. The crystal structure of hydrozincite, $Zn_6(OH)_6(CO_3)_2$. Acta Crystallogr 1964;17:1051–7.
[37] Whitaker A. The crystal structure of hopeite, $Zn_3(PO_4)_2(H_2O)_4$. Acta Crystallogr Sect B 1975;31:2026–35.
[38] Payne MC, Teter MP, Allan DC, Arais TA, Joannopoulos JD. Iterative minimization techniques for abinitio total-energy calculations – molecular-dynamics and conjugate gradients. Rev Mod Phys 1992;64:1045–97.
[39] Monkhorst HJ, Pack JD. Special points for brillouin-zone integrations. Phy Rev B 1976;13:5188–92.
[40] Perdew J, Burke K, Ernzerhof M. Generalized gradient approximation made simple. Phys Rev Lett 1996;77:3865–8.
[41] Porter AE. Ultrastructural comparison of hydroxyapatite and silicon substituted hydroxyapatite for bone graft applications, Ph.D. thesis, University of Cambridge; 2003.
[42] Sogo Y, Ito A, Fukasawa K, Sakurai T, Ichinose N. Zinc containing hydroxyapatite ceramics to promote osteoblastic cell activity. Mater Sci Technol 2004;20:1079–83.
[43] Chappell HF, Bristowe PD. Density functional calculations of the properties of silicon substituted hydroxyapatite. J Mater Sci Mater Med 2007;18: 829–37.
[44] Chappell H, Shepherd D, Best S. Zinc substituted hydroxyapatite – a comparison of modelling and experimental data. Key Eng Mater 2009;v396–v398: 729–32.
[45] Abrahams SC, Bernstain JL. Remeasurement of the structure of hexagonal ZnO. Acta Crystallogr Sect B 1969;25:1233–6.
[46] Hughes JM, Cameron M, Crowley KD. Structural variations in natural F, OH, and Cl apatites. Am Mineral 1989;74:870–6.
[47] Shannon RD. Revised effective ionic radii and systematic studies of interatomic distances in halides and chalcogenides. Acta Crystallogr 1976; A32:751–67.
[48] Trainor TP, Brown GE, Parks GA. Adsorption and precipitation of aqueous Zn(II) on alumina powders. J Colloid Interface Sci 2000;231:359–72.
[49] Elzinga EJ, Reeder RJ. X-ray absorption spectroscopy study of Cu^{2+} and Zn^{2+} adsorption complexes at the calcite surface: implications for site-specific metal incorporation preferences during calcite crystal growth. Geochim Cosmochim Acta 2002;66:3943–54.
[50] Roberts DR, Ford RG, Sparks DL. Kinetics and mechanisms of Zn complexation on metal oxides using EXAFS spectroscopy. J Colloid Interface Sci 2003; 263:364–76.
[51] Lee YJ, Elzinga EJ, Reeder RJ. Sorption mechanisms of zinc on hydroxyapatite: systematic uptake studies and EXAFS spectroscopy analysis. Environ Sci Technol 2005;39:4042–8.
[52] Pan Y, Fleet ME. Compositions of the apatite-group minerals: substitution mechanisms and controlling factors. In: Kohn M, Rakovan J, Hughes JM, editors. Phosphates: geochemical, geobiological and materials importance. Reviews in mineralogy and geochemistry, 48. Washington, DC: Mineralogical Society of America; 2002. p. 13–50.
[53] Barralet J, Best S, Bonfield WJ. Carbonate substitution in precipitated hydroxyapatite: an investigation into the effects of reaction temperature and bicarbonate ion concentration. Biomed Mater Res 1998;41:79–86.